RESEARCH ARTICLE

NANO · MICRO small
www.small-journal.com

Understanding the Role of Imide-Based Salts and Borate-Based Additives for Safe and High-Performance Glyoxal-Based Electrolytes in Ni-Rich NMC_{811} Cathodes for Li-Ion Batteries.

Michel Klein, Markus Binder, Matjaž Koželj, Adriano Pierini, Tom Gouveia, Thomas Diemant, Annika Schür, Sergio Brutti, Enrico Bodo, Dominic Bresser, Juan Luis Gómez-Urbano, and Andrea Balducci**

Herein, the design of novel and safe electrolyte formulations for high-voltage Ni-rich cathodes is reported. The solvent mixture comprising 1,1,2,2-tetraethoxyethane and propylene carbonate not only displays good transport properties, but also greatly enhances the overall safety of the cell thanks to its low flammability. The influence of the conducting salts, that is, lithium bis(trifluoromethanesulfonyl)imide (LiTFSI) and lithium bis(fluorosulfonyl)imide (LiFSI), and of the additives lithium bis(oxalato)borate (LiBOB) and lithium difluoro(oxalato)borate (LiDFOB) is examined. Molecular dynamics simulations are carried out to gain insights into the local structure of the different electrolytes and the lithium-ion coordination. Furthermore, special emphasis is placed on the film-forming abilities of the salts to suppress the anodic dissolution of the aluminum current collector and to create a stable cathode electrolyte interphase (CEI). In this regard, the borate-based additives significantly alleviate the intrinsic challenges associated with the use of LiTFSI and LiFSI salts. It is worth remarking that a superior cathode performance is achieved by using the LiFSI/LiDFOB electrolyte, displaying a high specific capacity of 164 mAh g^{-1} at 6 C and ca. 95% capacity retention after 100 cycles at 1 C. This is attributed to the rich chemistry of the generated CEI layer, as confirmed by ex situ X-ray photoelectron spectroscopy.

1. Introduction

Lithium-ion batteries (LIBs) were first commercialized by Sony in 1991 and have since been constantly improved, becoming ubiquitous in various applications such as electronic portable devices or road-based transport.[1] Despite their widespread use, safety remains a paramount concern. This is especially true for high-energy LIBs, where the large voltage employed can seriously compromise the stability of cell components, enhancing greatly the fire and explosion risks.[2] In this regard, great efforts are made today to further increase the safety of commercial LIBs, in addition to existing mechanisms such as safety vents or separators which stops the ionic transport at ≈130 °C.[3] In this context, the electrolyte is a key component for achieving greater safety.[4] The current state-of-the-art electrolyte comprises a liquid organic system consisting primarily of a binary solvent mixture and a lithium conducting salt.

M. Klein, J. L. Gómez-Urbano, A. Balducci
Institute for Technical Chemistry and Environmental Chemistry
Friedrich-Schiller University Jena
Philosophenweg 7a, 07743 Jena, Germany
E-mail: juanlu.gomez.urbano@uni-jena.de; andrea.balducci@uni-jena.de

M. Klein, J. L. Gómez-Urbano, A. Balducci
Center for Energy and Environmental Chemistry Jena (CEEC)
Friedrich-Schiller University Jena
Philosophenweg 7a, 07743 Jena, Germany

The ORCID identification number(s) for the author(s) of this article can be found under https://doi.org/10.1002/smll.202401610

DOI: 10.1002/smll.202401610

M. Binder, T. Diemant, A. Schür, D. Bresser
Helmholtz Institute Ulm (HIU) Electrochemical Energy Storage
Helmholtzstrasse 11, 89081 Ulm, Germany

M. Binder, T. Diemant, A. Schür, D. Bresser
Karlsruhe Institute of Technology (KIT)
P.O. Box 3640, 76021 Karlsruhe, Germany

M. Koželj, T. Gouveia
Solvionic
11 Chemin des Silos, Toulouse 31100, France

A. Pierini, S. Brutti, E. Bodo
Department of Chemistry
Sapienza University of Rome
Piazzale Aldo Moro 5, Rome 00185, Italy

S. Brutti
Consiglio Nazionale delle Ricerche
Istituto dei Sistemi Complessi
Piazzale Aldo Moro 5, Rome 00185, Italy

Conventional solvent blends are generally formed by a cyclic carbonate (e.g., ethylene carbonate (EC)) and a linear carbonate (e.g., dimethyl carbonate (DMC)). Lithium hexafluorophosphate ($LiPF_6$) is commonly used as conducting salt.[5] $LiPF_6$ offers high ionic conductivity, the ability to passivate the Al current collector at the cathode, and facilitates the formation of an effective solid electrolyte interphase (SEI).[1c,3b] However, $LiPF_6$, is in an endothermal equilibrium with its decomposition products LiF and PF_5.[6] The emerging LiF is poorly soluble in the organic solvents (EC: 5.52 g L^{-1}; DMC: 0.57 g L^{-1}), whereas the PF_5 is gaseous and can react with traces of water, leading to the release of HF.[7] On the other hand, linear carbonates like DMC have a low flash point (ca. 15 °C), enhancing gravely the fire risk of the cell.[8] Thus, one possible strategy toward improved safety would rely on the replacement of $LiPF_6$ and the linear carbonates. A promising alternative to $LiPF_6$ are the well-known imide-based conducting salts lithium bis(trifluoromethanesulfonyl)imide (LiTFSI) and lithium bis(fluorosulfonyl)imide (LiFSI).[3b,9] Compared to $LiPF_6$ these salts feature a better thermal and chemical stability and favorable attributes for LIBs with extended lifespan such as a high associated conductivity and good solvation ability.[10] Also, these imide-based salts present substantially enhanced safety features, displaying a considerably lower sensitivity toward hydrolysis compared to $LiPF_6$. While LiTFSI presents a wider stability than LiFSI, its high price renders it currently unaffordable for large-scale adoption.[11] In contrast, LiFSI has garnered attention from major battery manufacturers, since its large-scale production was started in 2013. In fact, it has been widely used as an additive for fast charging LIBs and its portion in commercial electrolyte formulations gradually increases as its price, which in 2021 was lower than the current price of $LiPF_6$, is further reduced.[12] Moreover, it is worth remarking that the lower percentage of fluorine in the LiFSI molecule positively impacts its environmental assessment. On the solvent side, 1,1,2,2-tetraethoxyethane (TEG) was investigated in an earlier publication as a possible candidate for use in LIBs due to its comparable viscosity (1.74 mPa s at 20 °C) and dielectric constant (2.55) to DMC but improved safety features such as a wide liquidus range (−35–220 °C) and lower flammability (flash point of 71 °C).[8] In addition, TEG has demonstrated film-forming properties in combination with graphite electrodes.[13]

In this study, we investigated different electrolyte formulations based on a binary solvent mixture comprising TEG and propylene carbonate (PC) in combination with LiFSI or LiTFSI as conducting salts. Since imide-based salts have been shown to promote the anodic dissolution of the aluminum current collector, the use of LiBOB and LiDFOB as additives was examined.[14] LiBOB not only shows reduced reactivity toward water and lower toxicity but also good electrochemical stability and the ability to passivate the aluminum current collector.[15] LiDFOB combines the properties of LiBOB and $LiBF_4$ featuring a higher ionic conductivity than LiBOB and a comparable ability to passivate the aluminum current collector. Furthermore, both show a higher thermal stability compared to $LiPF_6$.[16] In the first part of the manuscript, the viscosity, conductivity, electrochemical stability (ESW) of the investigated electrolytes and their ability to passivate the aluminum current collector are studied. Furthermore, computational studies are carried out to gain insight into the coordination and transport of the lithium cations in the different electrolytes. In the second part, we investigate their use in combination with NMC_{811} cathodes, carefully analyzing the influence on the rate capability tests and cycling stability of this high-energy cathode material as well as the chemistry of the cathode electrolyte interphase (CEI).

2. Results and Discussion

2.1. Electrolyte Characterization

The electrolytes were formulated with 1 M LiTFSI or LiFSI in a solvent blend of TEG/PC (3:7). Additionally, 2 wt% of LiBOB or LiDFOB were incorporated into these solutions to assess their impact on the electrolyte properties. The viscosity of the electrolytes was investigated across a temperature range from −10 to 50 °C, as shown in **Figure 1a**. As expected, in all cases their viscosity decreased with increasing temperature. The electrolytes containing LiTFSI as the primary conducting salt displayed higher viscosity compared to those with LiFSI. The introduction of 2 wt% of LiBOB and LiDFOB salts lead to a slight increase in viscosity. Specifically, viscosity values of 9.56 and 9.04 mPa s at 20 °C were measured for LiTFSI and LiFSI electrolytes, respectively. After adding LiBOB or LiDFOB, viscosity values changed to ca. 11.57 and 10.72 mPa s for the LiTFSI and LiFSI-based electrolytes, respectively (**Table 1**). On the other hand, the conductivity values of the electrolyte solutions (Figure 1b) follow the exact opposite trend as the viscosity for varying temperatures. Furthermore, the LiFSI-based electrolytes exhibited higher conductivity values than their LiTFSI counterparts (5.31 vs 3.42 mS cm^{-1} @20 °C). Also, the use of the borate additives led to a decrease in conductivity, viz., 3.33 and 4.75 mS cm^{-1} for LiTFSI and LiFSI, respectively (Table 1). In summary, the trend regarding favorable conductivity and viscosity values is the following: LiFSI > LiFSI/LiDFOB > LiFSI/LiBOB > LiTFSI > LiTFSI/LiDFOB >LiTFSI/LiBOB.

In terms of safety, the solvent mixture comprising TEG and PC ensures a flash point (f_p) above 73 °C for all the electrolytes, indicating a lower flammability compared to standard formulations such as 1 M $LiPF_6$ in EC/DMC (LP30, f_p: 31 °C). Notably, the LiTFSI-based electrolytes exhibit higher f_p values than their LiFSI counterparts, and the addition of lithium orthoborate salts leads to a slight decrease in the f_p. All investigated electrolytes display lower density values at 20 °C (ca. 1.2 g mL^{-1}) than LP30, potentially reducing the electrolyte's weight contribution by ≈10%, thus enhancing the overall specific energy of the device. It is worth mentioning that the LiTFSI-containing electrolytes show slightly higher density values than their LiFSI-based counterparts (Table 1). In order to gain further insights into the dynamic properties of the electrolytes, molecular dynamics simulations were performed for the 1 M LiTFSI and LiFSI electrolytes with and without the addition of 2 wt% LiBOB. For both LiTFSI and LiFSI electrolytes, the LiBOB additive causes a significant increase in the formation of closely interacting ion pairs. According to the data reported in **Figure 2a**, Li^+ cations surrounded exclusively by solvent molecules are significantly less abundant in both electrolytes containing LiBOB. In fact, the probability for Li^+ to be solvated exclusively by PC molecules decreases upon LiBOB addition from 43% to 34% and from 48% to 37% for LiTFSI and LiFSI respectively. At the same time, the probability of a TEG molecule being in the first Li^+ shell does not rise but instead decreases

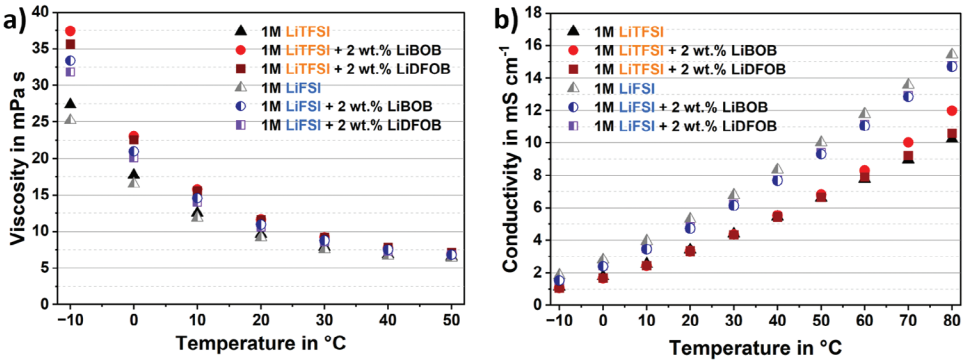

Figure 1. a) Viscosity and b) conductivity values measured as a function of temperature for the different electrolyte compositions.

slightly. Overall, the increase of the number of anions directly coordinating Li^+ in the LiBOB containing mixtures is increased by poorly dissociated Li^+-BOB^- ion pairs. Figure 2b shows that, despite the stoichiometric ratios of the salts (≈1:7 for BOB:TFSI and ≈1:8 for BOB:FSI), BOB anions display a large probability of residing inside the Li^+ solvation shell (green rows in Figure 2b). It is worth noting that only in the case of the LiTFSI + 2 wt% LiBOB electrolyte, the dissociation of the LiTFSI salt slightly decreased (Figure 2b, orange rows). Additionally, owing to the symmetric distribution of its coordinating sites, multiple Li^+ cations can be coordinated by one BOB^- at the same time Figure 2c,d. This can promote the formation of clustered local structures where BOB^- acts as a bridging unit between different ion pairs, which can ultimately represent a hindering factor for ionic transport across the electrolyte.

In sum, the decrease of the salt dissociation (and thus of "free" Li^+ ions) can be directly related to a decrease in conductivity. We would like to underline that, despite the systematic error in the calculated ionic diffusivities due to the unavoidable limitations of classical molecular dynamics (Figure S1, Supporting Information), their trend is in good agreement with the experimental conductivity values reported in Table 1. In fact, our modeling correctly predicts a more sluggish ionic transport in both the LiTFSI and LiFSI electrolytes after the addition of LiBOB. This effect is consistent with the lower degree of ionic dissociation and the promotion of clustered domains as observed in the structural analysis of the simulations.[17] Although not considered in the simulations, the same conclusions could be generically extended to the LiDFOB-added electrolytes, owing to the structural similarity of the two anions.

In the next step, the electrochemical stability of the electrolyte solutions was investigated by linear sweep voltammetry in order to confirm their compatibility with the high potentials required for the utilization of NMC_{811} electrodes. A current density threshold of ± 0.2 mA cm^{-2} was considered for determining the cathodic and anodic stability limits. As shown in **Figure 3a**, the 1 M LiTFSI electrolyte without additives presented the greatest stability against oxidation (5.1 V vs Li^+/Li) and reduction (0.03 V vs Li^+/Li) due to the large electrochemical stability of this salt. Introducing LiBOB or LiDFOB to LiTFSI-based electrolytes resulted in a shrinkage of the stability window, especially toward reduction, which shifted to ca. 0.2 V versus Li^+/Li. Conversely, the 1 M LiFSI electrolyte (Figure 3b) displayed a narrower stability window, ranging from 4.9 to 0.32 V versus Li^+/Li. In this case, the presence of the additives did not significantly change the stability toward reduction or oxidation. Considering these results, all electrolytes appear sufficiently stable at high potentials to be employed with Ni-rich cathode materials like NMC_{811}.

As discussed in the introduction, imide-based salts typically do not display a good ability to prevent the occurrence of anodic dissolution on the Al current collectors. In order to determine at which potential anodic dissolution processes start to take place

Table 1. Overview of the flash points, viscosity, conductivity, and density values at 20 °C as well as the stability toward oxidation and reduction of the different electrolyte systems.

Electrolyte	Viscosity [mPa s]	Conductivity [mS cm^{-1}]	Flash Point [°C]	Density [g mL^{-1}]	Ox. potential [V vs Li^+/Li]	Red. potential [V vs Li^+/Li]
1 M LiTFSI	9.56	3.42	92	1.24	5.1	0.03
1 M LiTFSI / LiBOB	11.63	3.33	80	1.25	5.0	0.21
1 M LiTFSI / LiDFOB	11.52	3.33	74	1.25	4.7	0.20
1 M LiFSI	9.04	5.31	87	1.20	4.9	0.32
1 M LiFSI / LiBOB	10.82	4.72	74	1.21	4.8	0.14
1 M LiFSI / LiDFOB	10.60	4.79	73	1.21	5.0	0.23
LP30[a)]	4.44	10.7	31	1.27 (25 °C)	–	–

[a)] The values in the table for the LP30 electrolyte were extracted from reference.[18]

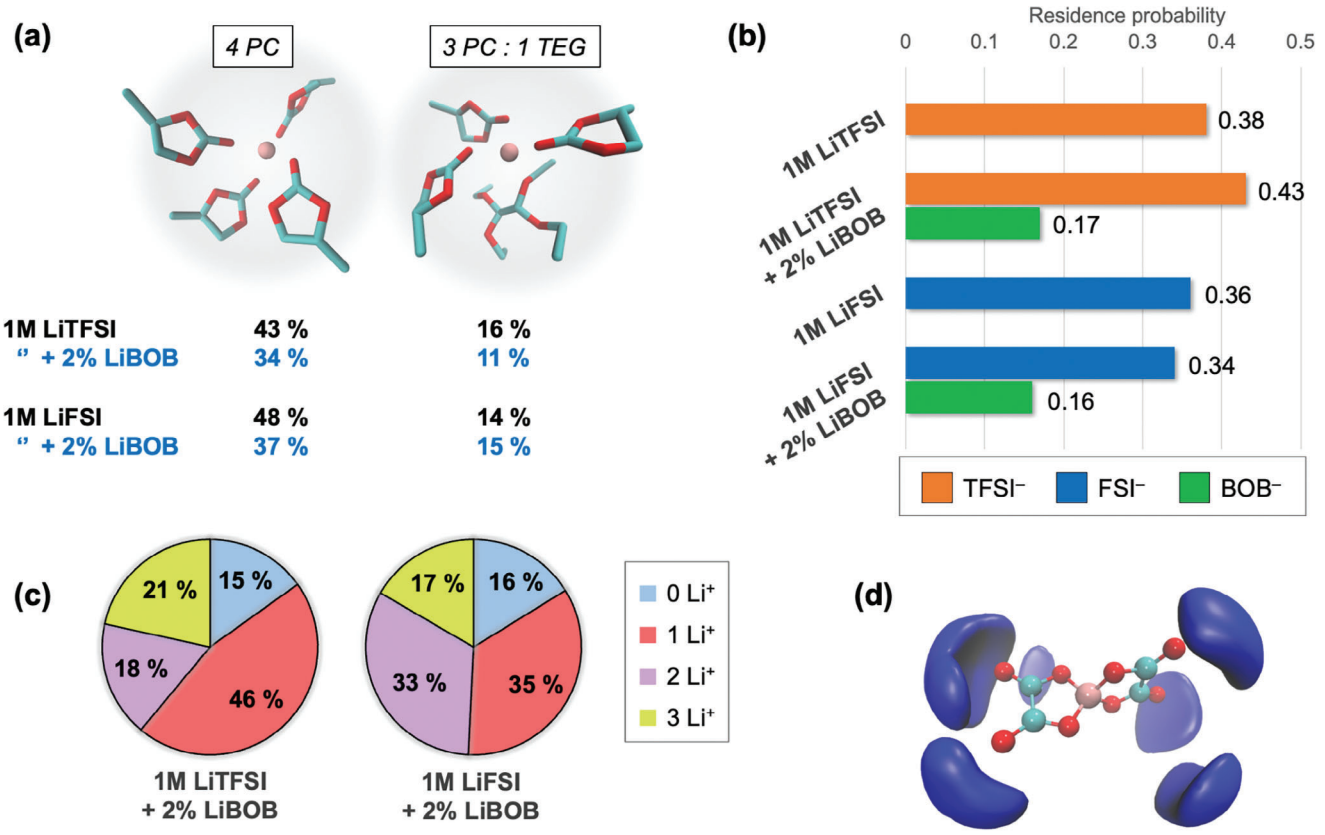

Figure 2. Structural data from the MD simulations: a) average probability (as percentage) of solvent-only configurations in the first solvation shell of Li^+, for the four different electrolytes; b) time-averaged residence probability of the TFSI/FSI/BOB anions in the first solvation shell of Li^+, expressed as the fraction of simulation time where the cation is surrounded by at least one (or more) anion of a same specie; c) average probability (as percentage) of finding one BOB anion coordinating up to three Li^+ cations; d) spatial distribution function of Li^+ cations around the BOB anion.

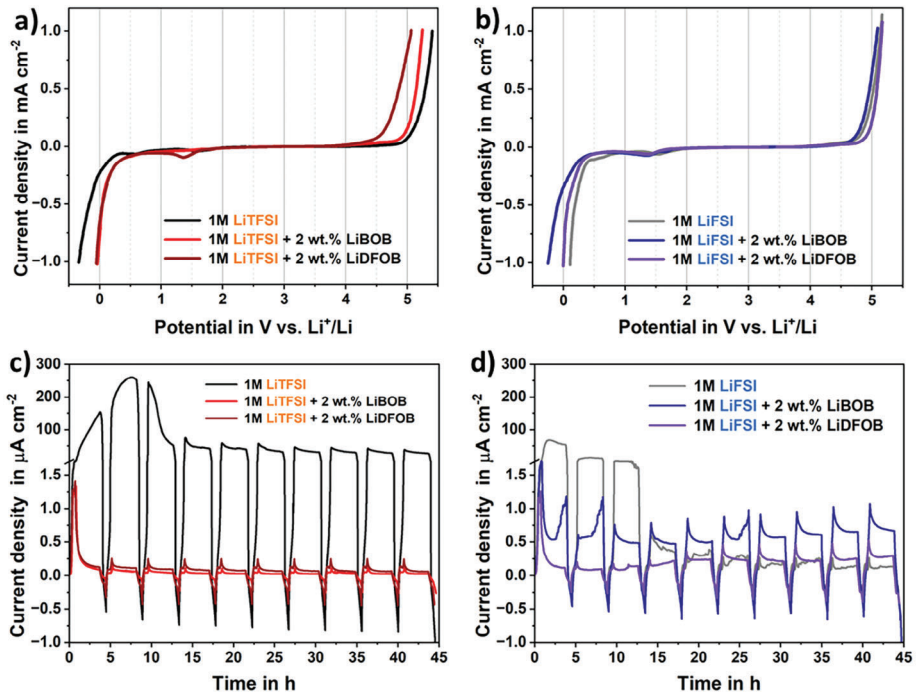

Figure 3. a,b) ESW test and c,d) current evolution response from the anodic dissolution tests performed with the different electrolyte systems.

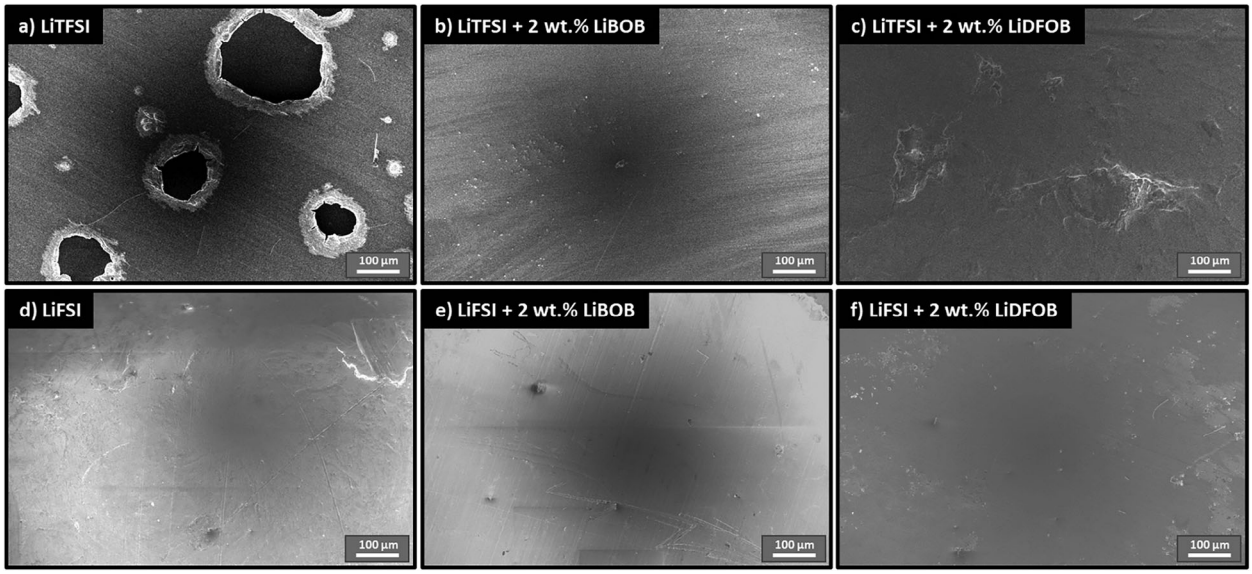

Figure 4. SEM images of Al discs after anodic dissolution tests at 4.3 V versus Li^+/Li in a) LiTFSI, b) LiTFSI/LiBOB, c) LiTFSI/LiDFOB, d) LiFSI, e) LiFSI/LiBOB and f) LiFSI/LiDFOB electrolyte.

in presence of the herein investigated electrolytes, a staircase potential-step chronoamperometry test was carried out from the OCV to positive potentials with uncoated aluminum discs (Figure S2, Supporting Information). The exponential increase in current observed at a certain potential can be related to several electrochemical processes such as the anodic dissolution of the aluminum current collector, the passivation of the aluminum current collector, or the decomposition of the electrolyte itself. In the case of 1 M LiTFSI and LiFSI electrolytes without additives, an exponential current evolution was recorded at 4.2 and 4.3 V versus Li^+/Li, respectively. These values are much lower than those measured in ESW measurements in which an inert surface (Pt) is employed. Thus, the exponential evolution in current recorded at these potentials can be ascribed to the initiation of parasitic reactions, which are usually ascribed to the anodic dissolution of the Al current collector.[3b,9] However, when LiBOB or LiDFOB additives were added, the current evolution showed a different trend and coincided well with the oxidation potential limits estimated in the ESW tests. These results indicate that the lithium orthoborate additives can effectively suppress the anodic dissolution of the aluminum current collector. To further investigate the phenomenon of anodic dissolution, a more severe test consisting of sequentially applying a constant potential of 4.3 V versus Li^+/Li to uncoated aluminum discs was carried out. The current responses caused by the polarization of pristine aluminum disks in contact with LiTFSI and LiFSI-based electrolytes are shown in Figure 3c,d, respectively. A high current evolution related to aluminum corrosion can be seen for 1 M LiTFSI electrolyte when no additive was employed (Figure 3c), due to the inability of LiTFSI to form a passivation layer on aluminum surface. Interestingly, the 1 M LiFSI electrolyte (Figure 3d) shows a large current evolution in the first cycles that is subsequently reduced until no current associated with anodic dissolution is detected anymore. It is important to note that there is still certain controversy regarding the possible passivation abilities of pure LiFSI at potentials of ca. 4.2 V versus Li^+/Li. Nevertheless, the effectiveness of this passivation is unclear.[10b] Considering the LiTFSI-based electrolyte formulations including LiBOB or LiDFOB, no significant current associated with anodic dissolution was detected in combination with the Al foil. Indeed, the higher current evolution observed in the first cycle for these electrolytes can be related to the decomposition of the additives to form a protective layer on the aluminum surface. This result further confirms the ability of the borate additives to prevent aluminum corrosion, even when the potential is held at 4.3 V versus Li^+/Li.[3b,16,19] On the other hand, a slightly higher current evolution is measured for the LiFSI-based formulations. This increase in current could be related to the corrosion of the stainless steel components of the cell, since this phenomenon also occurs when using the LiTFSI salt, but not as pronounced as with LiFSI, as reported elsewhere.[20]

The Al discs employed in the anodic dissolution tests at 4.3 V versus Li^+/Li were recovered and examined by scanning electron microscopy (SEM), the corresponding results are shown in **Figure 4**. The existence of large pits (Figure 4a) corroborates the inability of LiTFSI to form a passivation layer on aluminum.[21] In contrast and in good agreement with the current evolution recorded, no significant signs of corrosion were detected when the rest of the electrolytes were employed (Figure 4b–f).

2.2. Electrochemical Characterization of NMC_{811}

After the physicochemical characterization of the electrolytes, their impact on the electrochemical performance of NMC_{811} electrodes was investigated by galvanostatic charge/discharge cycling. The voltage profiles of the first cycle (at 0.05 C) of the NMC_{811} electrodes with the electrolyte formulations without additives are shown in Figure S3a (Supporting Information). The lower initial CE of the 1 M LiTFSI electrolyte can be mainly

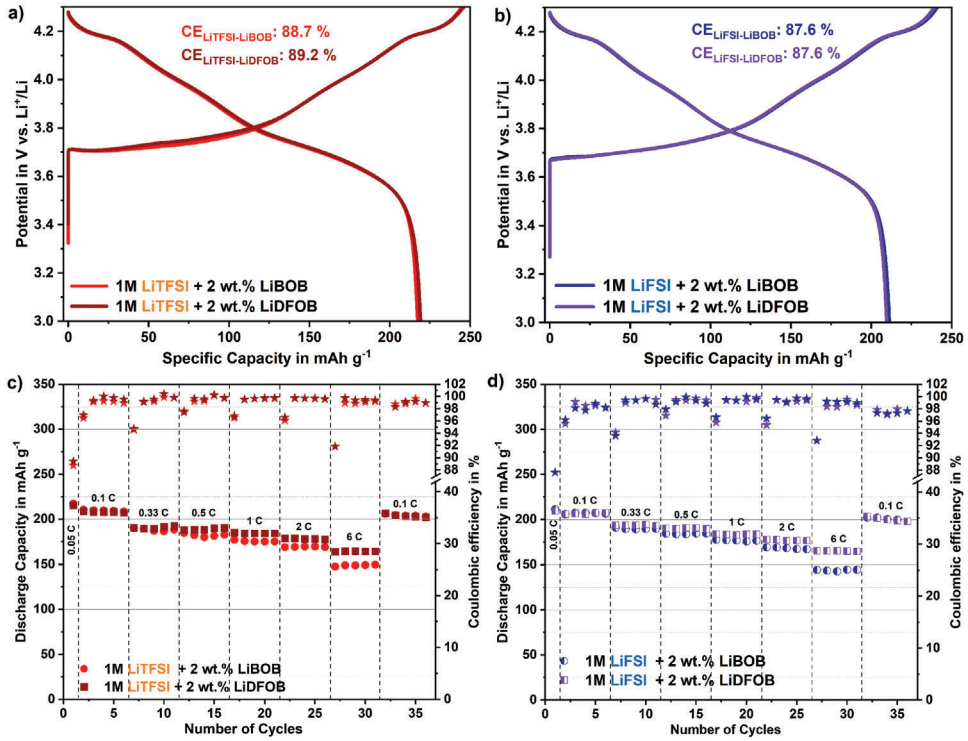

Figure 5. First galvanostatic charge/discharge cycle of NMC_{811} electrodes in half-cell configuration versus metallic lithium using a) LiTFSI- and b) LiFSI-based electrolytes. Also, rate capability tests at 0.05 C, 0.1 C, 0.33 C, 0.5 C 1 C, 2 C, 6 C for c) LiTFSI- and d) LiFSI-based electrolytes.

ascribed to the corrosion of the Al current collector. On the other hand, for the 1 M LiFSI electrolyte, an infinite plateau is observed at ca. 4.2 V versus Li^+/Li and consequently the upper potential limit (4.3 V vs Li^+/Li) is not reached. This phenomenon could be related to the anodic dissolution of the current collector. However, this plateau is not observed for the case of the 1 M LiTFSI electrolyte, which could indicate that the LiFSI salt is reacting with the stainless steel components of the cell. Further research, which falls out of the scope of the current study, would be needed to elucidate the origin of this process. These parasitic reactions are no longer observed in the first cycle when the LiBOB or LiDFOB additives are included in the electrolyte formulations (**Figure** 5a,b). In these cases, initial coulombic efficiency values reach almost 90% for both the LiTFSI and LiFSI-based formulations. The rate capability tests performed for the LiTFSI-based electrolytes are shown in Figure S3b (Supporting Information) (without additives) and Figure 5c. As expected, the worst capacity retention and CE values were observed for the 1 M LiTFSI due to its inability to avoid the anodic dissolution of the Al current collector. On the contrary, the addition of LiBOB or LiDFOB enables a suitable electrochemical performance up to a C-rate of 6 C. In more detail, even 150 and 164 mAh g^{-1} are retained at such a high dis-/charge rate for LiTFSI/LiBOB and LiFSI/LiDFOB, respectively. It is interesting to note that very similar electrochemical performance in terms of rate capability is achieved when using LiFSI instead of LiTFSI (Figure 5d). In this case, specific discharge capacities of 145 and 165 mAh g^{-1} are delivered at 6 C for LiFSI/LiBOB and LiFSI/LiDFOB, respectively. Nevertheless, slightly lower CE values are observed for LiFSI-based electrolytes when subsequently decreasing the C-rate to 0.1 C (ca. 97.5%) compared to that of LiTFSI (ca. 99%). Overall, the chosen additives seem to have a greater impact on the electrochemical performance than the primary salt itself. In this regard, the use of LiDFOB demonstrates to systematically enhance the capacity of the NMC_{811} half-cell at high rates.

Galvanostatic charge/discharge curves from the rate capability tests of the electrolyte formulations with additives are shown in Figure S4 (Supporting Information). All the curves show the characteristic signature profiles related to NMC_{811} cathodes. However, it is worth noting that the LiBOB additive leads to a slightly higher polarization when compared to that of LiDFOB, especially at elevated rates. The corresponding differential capacity plots presented in Figure S5 (Supporting Information) display the potentials at which the charging plateaus of the NMC_{811}-electrodes typically occur (≈3.63, 3.75, 4.0, and 4.2 V) as well as the corresponding discharging plateaus (≈3.73, 3.99, and 4.17 V).[22] While these features keep their position for the electrolytes with borate additives, a gradual shift was observed in the case of the 1 M LiTFSI electrolyte, which is due to the polarization caused by the anodic dissolution of the current collector. The long-term stability of the electrolytes in combination with NMC_{811} cathode materials was evaluated as depicted in **Figure 6**. While the 1 M LiTFSI electrolyte without additives presents a poor coulombic efficiency and capacity retention (Figure S3c, Supporting Information), the addition of LiBOB or LiDFOB to 1 M LiTFSI resulted in stable galvanostatic cycling over 100 cycles at 1 C (Figure 6a). Similar performances were achieved with the LiFSI-based counterparts, as shown in Figure 6b. It is worth noting that for all the samples the overall CE was ca. 99.5% at 1 C. As previously observed from the rate capability tests, the incorporation of

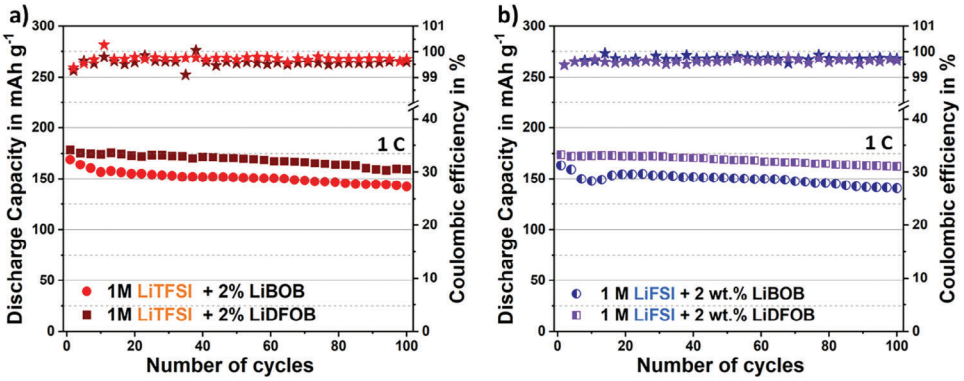

Figure 6. Long-term cycling of NMC_{811} electrodes at 1 C in half-cell configuration versus metallic lithium using a) LiTFSI- and b) LiFSI-based electrolytes containing borate-based additives.

LiDFOB significantly enhanced the electrochemical performance of the cells, leading to higher capacities.

The plot of the capacity retention upon cycling (Figure S6, Supporting Information) shows that LiDFOB seems not only to boost the capacity values but also to positively impact over retention. Also, a greater stability was observed for the cells containing LiFSI instead of LiTFSI in their formulation. More in detail, LiFSI/LiDFOB retained 93% of the initial capacity followed by LiTFSI/LiDFOB (90%), LiFSI/LiBOB (86%), and LiTFSI/LiBOB (84%). In sum, the results show that LiDFOB and LiFSI improve the capacity and stability of the NMC_{811} cathodes upon cycling. These results contrast with those reported by Li et al., in which LiTFSI in LiBOB featured a better stability.[23] It is worth remarking that the herein explored electrolytes outperform conventional 1 M $LiPF_6$ in EC:DMC electrolyte not only in terms of safety due to its lower flash point, but also with regard to capacity retention and rate capability (Figure S7, Supporting Information).

2.3. Ex Situ Characterization

The NMC_{811} electrodes were recovered after the long-term cycling test and further characterized to gain more insights into the electrode/electrolyte interactions. SEM images of pristine and cycled electrodes are depicted in Figure S8 (Supporting Information). Pristine electrodes show a homogenous distribution of the spherical-shaped NMC_{811} particles with a size of ca. 10 µm. Most of the particles retain their shape even if some fractures are observed as a result of the calendering process. No significant differences in terms of morphology can be found between the pristine and cycled electrodes after the long-term cycling tests regardless of the electrolyte employed. Ex situ X-ray powder diffraction (XRD) of the electrodes was also carried out to monitor possible structural distortions due to the cycling of the NMC_{811} materials. Refined XRD spectra are presented in Figure S9 (Supporting Information). No additional reflections were observed for the cycled electrodes, confirming the good structural stability of the material. Comparing the c/a ratio after galvanostatic cycling to the starting value of ca. 4.945 (**Table 2**), a slight increase can be found. This ratio expresses the hexagonal distortion in such layered materials and hence changes with the degree of lithiation.[24] Consequently, the increase of the c/a ratio is connected to the decreasing amount of lithium retained in the NMC structure after cycling. Thus, no clear features of material degradation can be observed within the structure of the NMC_{811} materials after long-term cycling when additives were employed. However, for the case of the 1 M LiTFSI sample without additives, the c/a ratio increased up to 5.1 after the cycling test. This could be ascribed to the inability of LiTFSI to form a stable CEI which led to a much more significant loss in active Li^+.

To study the chemical composition of the CEI, ex situ X-ray photoelectron spectroscopy (XPS) measurements were carried out. As expected, the electrode cycled with standard LP30

Table 2. Rietveld refined lattice parameters obtained from XRD data and goodness of fitting.

Sample	a	c	c/a	R_{wp}	GOF
NMC_{811} powder	2.870	14.195	4.945	1.63	1.94
Pristine NMC_{811} electrode	2.873	14.205	4.943	4.69	3.78
LP30	2.872	14.228	4.954	4.10	3.48
1 M LiTFSI-cycled	2.826	14.420	5.102	3.52	3.19
1 M LiTFSI/LiBOB-cycled	2.867	14.242	4.967	5.96	3.77
1 M LiTFSI/LiDFOB-cycled	2.869	14.228	4.958	5.27	3.65
1 M LiFSI/LiBOB-cycled	2.872	14.216	4.951	3.60	3.09
1 M LiFSI/LiDFOB-cycled	2.869	14.230	4.959	5.27	3.65

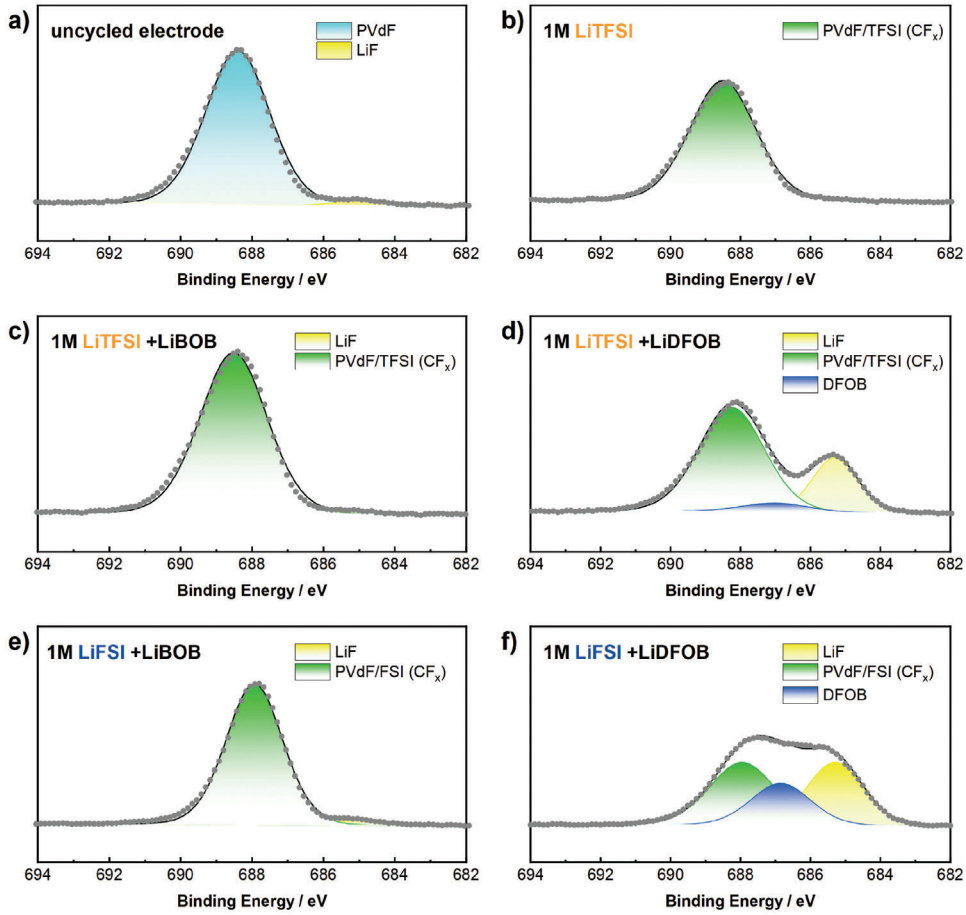

Figure 7. XPS detail spectra in the F 1s region recorded for NMC_{811} electrodes cycled in TEG/PC-based electrolytes. a) uncycled reference electrode, b) LiTFSI, c) LiTFSI/LiBOB, d) LiTFSI/LiDFOB, e) LiFSI/LiBOB and f) LiFSI/LiDFOB.

electrolyte showed C—O/C═O species, originating from the carbonate decomposition, and PO_xF_y/PF_z species from the $LiPF_6$ decomposition as main CEI components (Figure S10, Supporting Information).[25] Interestingly, the presence of oxidized boron species was also detected on the cycled LP30 cathode surface. These boron species were also present in the surface layer of the uncycled electrodes (Figure S14, Supporting Information), indicating that the commercial material had been modified by a boron-based surface coating.[26] For the comparison of the cathodes cycled using the TEG/PC-based electrolytes with the pristine, uncycled cathode and the one from the LP30 reference cell, the different elemental regions were plotted separately (**Figure 7**; Figures S11–S14, Supporting Information). First of all, the O 1s detail spectra in Figure S11 (Supporting Information) reveal for the cycled electrodes an increase of the peak at ≈533 eV, assigned to C–O species for the pristine sample. The increase is mainly related to the deposition of imide salts, which also contribute to this peak. In contrast, the M—O bond expresses the contribution of the NMC_{811} lattice, and hence, its intensity (more precisely its decrease) can be used as an indicator for CEI thickness. In general, the CEI after 100 cycles seems to be relatively thin for all the analyzed electrodes, as a distinct M—O peak is observed even though XPS is highly surface sensitive with a probing depth of ≈5 nm.[25a,b] Nevertheless, the normalized comparison (Table S1, Supporting Information) reveals that the M—O signal slightly decreases for LP30 and pure TFSI. A more pronounced reduction is observed for LiTFSI/LiBOB and LiTFSI/LiDFOB and the strongest for LiFSI/LiBOB and LiFSI/LiDFOB. This suggests that the electrolytes containing LiFSI as the main conductive salt and employing an additive can cover the active material more homogenously and form a thicker/denser CEI, resulting in a superior electrochemical performance. In addition, the normalized intensities of the sulfur signal provide insights into the incorporation of the imide salts into the CEI layer. In agreement with the previous findings, pure TFSI has the strongest signal. Furthermore, it is the only electrolyte system where decomposition products like LiNSO can be detected.[27] In all other cases, only the peak doublet of TFSI/FSI appears in the S 2p spectra (Figure S13, Supporting Information) which, however, varies in intensity.[27] Comparing the results for the two additives, LiBOB containing electrolytes lead to higher and LiDFOB to lower sulfur contribution. This trend is opposite to what is found for the boron amount (Figure S14, Supporting Information). Hence, it appears as if the decomposition and integration of LiDFOB into the CEI reduces the amount of imide integration into the interphase. A holistic overview of the differences in CEI composition can be gained by analyzing the spectra in the F 1s region which are depicted in Figure 7. The best-performing electrolyte

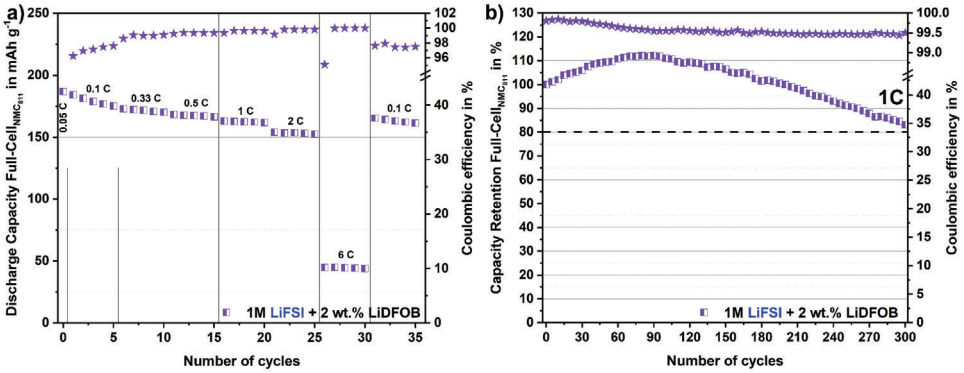

Figure 8. Electrochemical characterization of LIB full-cell assembled using NMC_{811} as positive electrode and graphite as negative electrode in the 1 M LiFSI/LiDFOB electrolyte including a) rate capability test at 0.05 C, 0.1 C, 0.33 C, 0.5 C, 1 C, 2 C, 6 C and, b) capacity retention along cycling at 1 C.

LiFSI/LiDFOB (cf. Figure S6, Supporting Information) clearly differs from the other electrolyte formulations. First, the decomposition of LiDFOB leads to a significant amount of LiF in the surface layer. Furthermore, the CEI contains also BF_x species (potentially still LiDFOB), which are particularly pronounced for the LiFSI/LiDFOB electrolyte.[28] The higher contribution of the additive LiDFOB comes together with a lower signal of CF_x species, coming from the conducting salt (compare S amount of LiFSI/LiBOB and LiFSI/LiDFOB in Table S1, Supporting Information) and (maybe) PVDF binder.

In summary, the ex situ XPS analysis confirmed the previous findings and showed that the additives reduce the decomposition of the conducting salt. The improved electrochemical performance with LiDFOB as an additive can be assigned to the stable LiF-rich CEI, which is unique for those two electrolyte systems. Accordingly, the better performance of 1 M LiFSI/LiDFOB can be related to its rich CEI that does not only include LiF, but also BF_x-species.

2.4. Lithium-Ion Battery

In view of the promising features of the 1 M LiFSI/LiDFOB electrolyte, its implementation in a LIB full-cell device was examined. First, its compatibility with graphite electrodes was assessed through galvanostatic cycling in a half-cell configuration versus metallic lithium (Figure S15, Supporting Information). The conventional lithium intercalation staging mechanism in graphite is confirmed by the appearance of three distinct plateaus. Despite the high proportion of PC in the electrolyte formulation, no solvent co-intercalation was observed. This suggests that the SEI formed by LiDFOB salt decomposition products inhibits the entrance of ion solvent-shells within graphite. The favorable compatibility between the LiFSI/LiDFOB electrolyte and the graphite electrodes was further confirmed by its enhanced capacity at high rates (300 mAh g^{-1} at 2 C) and low capacity fading along cycling (86.6% retention of the initial capacity after 200 cycles at 1 C). Subsequently, a LIB full-cell was assembled using the LiFSI/LiDFOB electrolyte with a graphite electrode as the negative electrode and a NMC_{811} electrode as the positive electrode. The device was galvanostatically charged/discharged at different rates as depicted in **Figure 8a**. Despite not being fully optimized, the device delivered 180 mAh g^{-1} at 0.1 C while still retaining over 150 mAh g^{-1} at 2 C. The capacity drop observed at 6 C can be ascribed to the sluggish kinetics of the Li^+ intercalation in the graphite anode (cf. Figure S15b, Supporting Information). Following the rate capability test, the cycle life of the LIB was evaluated by conducting 300 charge/discharge cycles at 1 C (Figure 8b). The device demonstrated good stability, retaining 83.1% of the initial capacity after 300 cycles. It is also worth highlighting that the coulombic efficiency values measured at 1 C remain above 99.5%. Overall, the aforementioned results underscore the promising features of the LiFSI/LiDFOB electrolyte as a viable candidate for its application in LIBs.

3. Conclusion

We hereby report the successful formulation of safe electrolytes compatible with nickel-rich NMC_{811} cathodes. The solvent mixture incorporating the glyoxal-based TEG solvent was first explored at high voltage regions, demonstrating smooth cell operation and enhanced safety due to its low associated flammability (flash point of electrolytes > 70 °C). The role of imide-based salts (LiTFSI, LiFSI) and borate additives (LiBOB, LiDFOB) was thoroughly examined. Molecular dynamics simulations provided insights into ion pair formations, suggesting reduced salt dissociation when the borate additives are incorporated. Electrochemical stability tests confirmed the compatibility of the electrolytes with the high potentials required for NMC_{811} electrodes while the anodic dissolution tests highlighted that the addition of LiBOB or LiDFOB guarantees a stable protection of the Al current collector, regardless of the imide-based salt employed. Moreover, electrolytes incorporating LiBOB or LiDFOB in a relatively low concentration demonstrated superior electrochemical performance in terms of rate capability and cycling retention compared to conventional electrolytes. Although similar performances were obtained for LiTFSI and LiFSI-based electrolytes, LiFSI exhibited greater stability during cycling. These results further underscore that LiFSI is a suitable candidate for high energy batteries, maybe even more than LiTFSI, since it does not only demonstrate better performance, but also a lower degree of fluorination and reduced price. The glyoxal-based electrolyte incorporating LiFSI and LiDFOB in its formulation demonstrated the best electrochemical performance, delivering even 165 mAh g^{-1} at 6 C with

93% capacity retention after 100 cycles at 1 C. The ex situ XPS characterization confirmed that these additives decrease the decomposition of the imide-based salts. The better performance of LiFSI/LiDFOB can be attributed to the rich chemistry of the generated CEI layer, incorporating LiF and BF_x species. Additionally, this electrolyte formulation was demonstrated to be compatible with graphite-based electrodes, delivering up to 350 mAh g^{-1} at 1 C in a half-cell configuration. Moreover, when used in a LIB full-cell it was possible to perform 300 charge/discharge cycles without reaching 80% of the initial capacity.

4. Experimental Section

Chemicals and Materials: The solvent TEG (CAS: 3975-14-2, Weylchem) was passed before use through a freshly activated alumina column (Brockman I) in order to remove the stabilizer and dried with freshly activated molecular sieves (4 Å) until water content was reduced below 1 ppm. After filtration, the solvent was ready for use. As-dried TEG and PC (CAS: 108-32-7, 99.9%, <20 ppm H_2O) were utilized to prepare a binary solvent mixture with a weight ratio of 3:7. LiFSI (CAS: 171611-11-3, 99.9%, <20 ppm H_2O) and LiTFSI (CAS: 90076-65-6, 99.9%, <20 ppm H_2O) as well as the additives LiBOB (CAS: 244761-29-3, 99.9%, <20 ppm H_2O) and LiDFOB (CAS: 409071-16-5, 99.9%, <20 ppm H_2O) were provided by Solvionic. In addition, a solution of 1 M $LiPF_6$ in EC:DMC (1:1 vol%) provided by Solvionic was also used as a reference electrolyte. Metallic lithium employed in this study was purchased from China Energy Lithium Co., Ltd.

Physicochemical Characterization: Viscosity measurements were carried out with a MCR 102 Rheometer equipped with a CP50-0.5 cone-plate system from Anton Paar in a temperature range of −20–50 °C with a constant shear rate of 1000 s^{-1}. The sample (0.5 mL) application was done at 20 °C. The conductivity of the electrolytes was measured with a Modulab XM ECS potentiostat in combination with a Binder MK53 climate chamber. Alternating current resistance was determined within a temperature range from −30 to 80 °C in a conductivity cell consisting of two parallel platinum electrodes. The determination was done at open circuit voltage by applying an alternating voltage with an amplitude of 5 mV, within a frequency range from 300 kHz to 1 Hz. The electrolyte volume for each measurement was 0.5 mL. Forming the reciprocal of the alternating current resistance gives the conductance. The conductivity values were obtained after multiplying the as-obtained conductance by the known-cell constant. The cell constant was determined by employing a 3 M KCl solution.

Densities of the electrolytes were determined by an Anton Paar DMA 4100 density meter (oscillating U tube principle). Flash points were determined by an Eraflash automated flash point tester, using the continuously closed cup flash point testing method according to ASTM D7094.

Electrodes and Cell Preparation: NMC_{811} electrodes were prepared using 92 wt% commercial NMC_{811}, 4 wt% conductive carbon (CNERGY Super C65, Imerys), and 4 wt% polyvinylidene difluoride (PVdF, Solef 6020, Solvay) binder. The slurry was mixed with a planetary mixer (ARE-250, Thinky) and cast with a wet film thickness of 60 µm on battery-grade aluminum foil inside a dry room, dried at 120 °C for 12 h, and eventually calendered to a target porosity of 30%. The water-based graphite electrodes consisted of 90 wt% graphite (C-NERGY Actilion GHDR 15-4, Imerys), 5 wt% conductive carbon Super C65 (C-NERGY, Imerys) and 5 wt% carboxymethyl cellulose (Walocel CRT 2000 PA, DuPont). The mixture, with a solid-to-liquid weight ratio of 3 to 7, was homogenized via ball milling and subsequently cast with a wet film thickness of 100 µm on copper foil. The film was dried overnight under a vacuum at 70 °C. Circular-shaped electrodes of 12 mm diameter were punched out under argon atmosphere. The resulting electrodes displayed an active material mass loading in the range from 2.5 to 3.5 mg cm^{-2} for NMC_{811} and from 2.1 to 3.1 mg cm^{-2} for graphite. The electrochemical measurements were conducted using Swagelok-type cells. Circular Whatman GF/D glass microfiber filter sheets (CAT-No. 1823-150, 13 mm diameter) soaked with an electrolyte volume of 150 µL acted as separator between the working and counter electrode. In the case of the three-electrode setup, an additional glass microfiber filter (8 mm diameter) was utilized as separator between the working/counter and reference electrodes. Cells were assembled in an argon-filled MBraun glovebox Lab Master Pro Eco (H_2O concentration: < 0.1 ppm, 0_2 concentration: < 0.1 ppm).

Electrochemical Measurements: The electrochemical stability window of the electrolyte was analyzed using linear sweep voltammetry at 5 mV s^{-1} (± 0.2 mA cm^{-2} current threshold). For this purpose, a Pt disc (with well-defined diameter) was used as working electrode, a silver wire as quasi-reference electrode, and a graphite rod as counter electrode. Separate LSV tests were conducted to determine the corresponding anodic and cathodic stability limits and ferrocene was used as internal standard for accurate potential determination.

In addition, sequences of chronoamperometric measurements were carried out to investigate the onset potential of the electrochemical reactions (anodic dissolution) at an aluminum working electrode. For this purpose, the potential was gradually increased by 0.1 V increments from 3.5 V versus Li^+/Li to 5 V versus Li^+/Li, with a holding time of one hour for each potential step and recording the current response. These tests were performed in coin type cells, using lithium metal as anode (reference and counter electrode), a glass fiber separator soaked with the corresponding electrolyte, and a disc of aluminum as cathode (working electrode). Anodic dissolution tests were also performed in a three-electrode configuration employing an aluminum disk as working electrode and lithium metal discs as counter and reference electrodes. The potential of the aluminum discs was scanned at 0.5 mV s^{-1} between 3.0 and 4.3 V versus Li^+/Li and held for 3 h at the upper potential limit in each cycle. A total of ten cycles were performed while the resulting current was recorded. NMC_{811} as well as graphite electrodes were evaluated in a half-cell configuration using a two-electrode setup. In these measurements, either a NMC_{811} or a graphite electrode was utilized as a working electrode and an oversized lithium metal electrode acted simultaneously as counter and reference electrode. Galvanostatic charge/discharge measurements were conducted at different C-rates, whereas 1 C corresponds to 200 mA g^{-1} for NMC_{811} and 350 mA g^{-1} for graphite. In the case of the NMC_{811} half-cells, an asymmetric charge/discharge protocol (between 3.0 and 4.3 V vs Li^+/Li) was followed for the C-rate tests, fixing the charge rate to 0.33 C and varying the discharge rate from 0.33 C to 0.5 C, 1 C, 2 C, and 6 C. For the graphite half-cells, a symmetrical charge/discharge protocol (between 0.01 and 1.0 V vs Li^+/Li) was applied. Long-term tests were performed after 6 activation cycles (1st cycle at 0.05 C and the subsequent 5 cycles at 0.1 C) using a charge/discharge rate of 1 C for 100 cycles. The LIB full-cell characterization was performed via symmetrical charge/discharge at different rates followed by a long-term test protocol (1 C:200 mA g^{-1}). The potential of the positive electrode was limited to 4.3 V vs Li^+/Li, the negative electrode potential was limited to 0.005 V vs Li^+/Li and the cell voltage was limited between 2.0 and 4.3 V. The capacity ratio of negative to positive electrode was 1.4. The measurements were performed using a BioLogic VMP-3 multichannel potentiostat. The specific capacity and current density values were calculated with respect to the total mass of the active material.

Ex Situ Characterization: After the anodic dissolution tests as well as the cycling stability tests, the Swagelok-type cells were disassembled inside an argon-filled glove box. The NMC_{811} and aluminum electrodes were soaked in PC for approximately one minute and subsequently dried under vacuum at 40 °C overnight in a glass oven B-585 from Büchi. SEM analysis was conducted using a Zeiss Crossbeam XB340 field-emission electron microscope equipped with an energy-dispersive X-ray (EDX) spectroscopy detector (Oxford Instruments X-Max Xtreme, 100 mm^2, 1–5 kV). For the SEM and EDX analysis, the acceleration voltage was set to 3 and 10 keV, respectively. XRD measurements were performed using a Bruker D8 Advance with Cu Kα radiation ($\lambda = 0.154$ nm). The obtained patterns were analyzed using TOPAS 5. Ex situ XPS measurements of cycled NMC electrodes were performed on a Specs XPS system with a Phoibos 150 energy analyzer. The spectra were acquired using monochromatized Al Kα radiation (400 W. 15 kV) and pass energies of 90 and 30 eV for the survey and the detail measurements, respectively. When necessary, sample charging

was neutralized with an electron flood gun, and the spectra were calibrated to the main C 1s peak at 284.8 eV of C—C/C—H species. To avoid surface contamination, the samples were transferred in inert gas atmosphere from the glove box to the sample load lock of the XPS system. The peak fit of the XPS data was done with CasaXPS, using Shirley-type backgrounds and Gaussian–Lorentzian peak shapes.

Molecular Dynamics Simulations: Atomistic simulations were performed using the LAMMPS code.[29] The classical OPLSS-AA force field was chosen to describe the bonded and non-bonded atomistic interactions, adopting the parameters from previous literature sources.[30] Coulomb interactions were scaled down by applying a relative permittivity $\epsilon = 1.2$, which is equivalent to the common practice of applying an empirical scaling factor of 0.8 to atomic fixed charges, in order to incorporate on average the effects of charge polarization of a liquid electrolyte system. The initial cubic cells of the electrolyte were optimized and relaxed using the isobaric (NPT) ensemble (at 293 K and 1 atm) for 5 ns. Thermalization at fixed volume in the isothermal (NVT) ensemble (T = 293 K) was performed for 10 ns, after which the statistical sampling was run for a total of 20 ns. Velocity-Verlet integrator with time-step of 1 fs was used, together with Nosée–Hoover barostat and thermostat for sampling in NPT and NVT ensemble. A cutoff value of 12 Å was applied to both van der Waals and Coulomb non-bonded interactions.

Supporting Information

Supporting Information is available from the Wiley Online Library or from the author.

Acknowledgements

The authors want to acknowledge the financial support of the European Union´s Horizon Europe transport program under the project SiGNE (grant agreement No 101069738). SB would like to also thank Sapienza for the financial support through the project RM122181677EDA1D. The authors would also like to acknowledge Susan Sananes Israel for her help regarding the formulation of the graphite electrodes.

Open access funding enabled and organized by Projekt DEAL.

Conflict of Interest

The authors declare no conflict of interest.

Data Availability Statement

The data that support the findings of this study are available from the corresponding author upon reasonable request.

Keywords

cathode, electrolyte, lithium salt, lithium-ion battery, NMC_{811}

Received: February 29, 2024
Revised: May 14, 2024
Published online:

[1] a) Y. Nishi, *Chem Rec* **2001**, *1*, 406; b) Z. P. Cano, D. Banham, S. Ye, A. Hintennach, J. Lu, M. Fowler, Z. Chen, *Nat. Energy* **2018**, *3*, 279; c) M. Armand, P. Axmann, D. Bresser, M. Copley, K. Edström, C. Ekberg, D. Guyomard, B. Lestriez, P. Novák, M. Petranikova, W. Porcher, S. Trabesinger, M. Wohlfahrt-Mehrens, H. Zhang, *J. Power Sources* **2020**, *479*, 228708.

[2] A. Mauger, C. M. Julien, *Ionics* **2017**, *23*, 1933.

[3] a) P. Arora, Z. Zhang, *Chem. Rev.* **2004**, *104*, 4419; b) J. Kalhoff, G. G. Eshetu, D. Bresser, S. Passerini, *ChemSusChem* **2015**, *8*, 2154.

[4] a) K. S. Teoh, M. Melchiorre, S. Darlami Magar, M. Hermesdorf, D. Leistenschneider, M. Oschatz, F. Ruffo, J. L. Gómez Urbano, A. Balducci, *Adv. Mater.* **2024**, *36*, 2310056; b) F. A. Kreth, L. Köps, C. Leibing, S. Darlami Magar, M. Hermesdorf, K. Schutjajew, C. Neumann, D. Leistenschneider, A. Turchanin, M. Oschatz, J. L. Gómez Urbano, A. Balducci, *Adv. Energy Mater.* **2024**, *14*, 2303909.

[5] K. Xu, *Chem. Rev.* **2004**, *104*, 4303.

[6] D. Aurbach, A. Zaban, Y. Ein-Eli, I. Weissman, O. Chusid, B. Markovsky, M. Levi, E. Levi, A. Schechter, E. Granot, *J. Power Sources* **1997**, *68*, 91.

[7] a) J. Jones, M. Anouti, M. Caillon-Caravanier, P. Willmann, D. Lemordant, *Fluid Phase Equilib.* **2009**, *285*, 62; b) H. Yang, G. V. Zhuang, P. N. Ross Jr, *J. Power Sources* **2006**, *161*, 573.

[8] L. H. Heß, A. Balducci, *ChemSusChem* **2018**, *11*, 1919.

[9] J. Kalhoff, D. Bresser, M. Bolloli, F. Alloin, J.-Y. Sanchez, S. Passerini, *ChemSusChem* **2014**, *7*, 2939.

[10] a) Z. Lu, L. Yang, Y. Guo, *J. Power Sources* **2006**, *156*, 555; b) H.-B. Han, S.-S. Zhou, D.-J. Zhang, S.-W. Feng, L.-F. Li, K. Liu, W.-F. Feng, J. Nie, H. Li, X.-J. Huang, *J. Power Sources* **2011**, *196*, 3623.

[11] T. F. Burton, R. Jommongkol, Y. Zhu, S. Deebansok, K. Chitbankluai, J. Deng, O. Fontaine, *Curr. Opin. Electrochem.* **2022**, *35*, 101070.

[12] Y. Cai, H. Zhang, Y. Cao, Q. Wang, B. Cao, Z. Zhou, F. Lv, W. Song, D. Duo, L. Yu, *J. Power Sources* **2022**, *535*, 231481.

[13] a) L. H. Hess, S. Wankmüller, L. Köps, A. Bothe, A. Balducci, *Batteries Supercaps* **2019**, *2*, 852; b) L. Köps, C. Leibing, L. H. Hess, A. Balducci, *J. Electrochem. Soc.* **2021**, *168*, 010513; c) C. Leibing, D. Leistenschneider, C. Neumann, M. Oschatz, A. Turchanin, A. Balducci, *ChemSusChem* **2023**, *16*, 202300161; d) M. Orbay, D. Leistenschneider, C. Leibing, A. Balducci, *ChemElectroChem* **2023**, *10*, 202300171.

[14] a) P. Meister, X. Qi, R. Kloepsch, E. Krämer, B. Streipert, M. Winter, T. Placke, *ChemSusChem* **2017**, *10*, 804; b) L. Nyholm, T. Ericson, A. S. Etman, *Chem. Eng. Sci.* **2023**, *282*, 119346.

[15] a) G. Hernández, R. Mogensen, R. Younesi, J. Mindemark, *Batteries Supercaps* **2022**, *5*, 202100373; b) S. Di Muzio, O. Palumbo, S. Brutti, A. Paolone, *J. Electrochem. Soc.* **2022**, *169*, 070523.

[16] S. S. Zhang, *Electrochem. Commun.* **2006**, *8*, 1423.

[17] N. Yao, L. Yu, Z. H. Fu, X. Shen, T. Z. Hou, X. Liu, Y. C. Gao, R. Zhang, C. Z. Zhao, X. Chen, Q. Zhang, *Angew. Chem., Int. Ed.* **2023**, *62*, 202305331.

[18] A. Hofmann, M. Migeot, E. Thißen, M. Schulz, R. Heinzmann, S. Indris, T. Bergfeldt, B. Lei, C. Ziebert, T. Hanemann, *ChemSusChem* **2015**, *8*, 1892.

[19] K. Xu, S. Zhang, T. R. Jow, W. Xu, C. A. Angell, *Electrochem. Solid-State Lett.* **2001**, *5*, A26.

[20] a) L. Wang, Z. Luo, H. Xu, N. Piao, Z. Chen, G. Tian, X. He, *RSC Adv.* **2019**, *9*, 41837; b) X. Wu, Z. Du, *Electrochem. Commun.* **2021**, *129*, 107088; c) C. Luo, Y. Li, W. Sun, P. Xiao, S. Liu, D. Wang, C. Zheng, *Electrochim. Acta* **2022**, *419*, 140353.

[21] a) L. J. Krause, W. Lamanna, J. Summerfield, M. Engle, G. Korba, R. Loch, R. Atanasoski, *J. Power Sources* **1997**, *68*, 320; b) K. Matsumoto, K. Inoue, K. Nakahara, R. Yuge, T. Noguchi, K. Utsugi, *J. Power Sources* **2013**, *231*, 234.

[22] a) H.-J. Noh, S. Youn, C. S. Yoon, Y.-K. Sun, *J. Power Sources* **2013**, *233*, 121; b) K. Märker, P. J. Reeves, C. Xu, K. J. Griffith, C. P. Grey, *Chem. Mater.* **2019**, *31*, 2545.

[23] X. Li, J. Zheng, M. H. Engelhard, D. Mei, Q. Li, S. Jiao, N. Liu, W. Zhao, J.-G. Zhang, W. Xu, *ACS Appl. Mater. Interfaces* **2018**, *10*, 2469.

[24] a) M. Bianchini, M. Roca-Ayats, P. Hartmann, T. Brezesinski, J. Janek, *Angew Chem Int Ed Engl* **2019**, *58*, 10434; b) Y. Ruan, X. Song, Y. Fu, C. Song, V. Battaglia, *J. Power Sources* **2018**, *400*, 539.

[25] a) M. Hekmatfar, A. Kazzazi, G. G. Eshetu, I. Hasa, S. Passerini, *ACS Appl. Mater. Interfaces* **2019**, *11*, 43166; b) M. Hekmatfar, I. Hasa, R. Eghbal, D. V. Carvalho, A. Moretti, S. Passerini, *Adv. Mater. Interfaces* **2020**, *7*, 1901500; c) Q. Dong, F. Guo, Z. Cheng, Y. Mao, R. Huang, F. Li, H. Dong, Q. Zhang, W. Li, H. Chen, Z. Luo, Y. Shen, X. Wu, L. Chen, *ACS Appl. Energy Mater.* **2020**, *3*, 695.

[26] a) W. Mo, Z. Wang, J. Wang, X. Li, H. Guo, W. Peng, G. Yan, *Chem. Eng. J.* **2020**, *400*, 125820; b) I. A. Skvortsova, E. D. Orlova, A. O. Boev, D. A. Aksyonov, I. Moiseev, E. M. Pazhetnov, A. A. Savina, A. M. Abakumov, *J. Power Sources* **2023**, *583*, 233571.

[27] F. Wu, S. Fang, M. Kuenzel, A. Mullaliu, J.-K. Kim, X. Gao, T. Diemant, G.-T. Kim, S. Passerini, *Joule* **2021**, *5*, 2177.

[28] a) S. Jiao, X. Ren, R. Cao, M. H. Engelhard, Y. Liu, D. Hu, D. Mei, J. Zheng, W. Zhao, Q. Li, *Nat. Energy* **2018**, *3*, 739; b) L. Dong, F. Liang, D. Wang, C. Zhu, J. Liu, D. Gui, C. Li, *Electrochim. Acta* **2018**, *270*, 426.

[29] A. P. Thompson, H. M. Aktulga, R. Berger, D. S. Bolintineanu, W. M. Brown, P. S. Crozier, P. J. in't Veld, A. Kohlmeyer, S. G. Moore, T. D. Nguyen, *Comput. Phys. Commun.* **2022**, *271*, 108171.

[30] a) M. Takeuchi, Y. Kameda, Y. Umebayashi, S. Ogawa, T. Sonoda, S.-i. Ishiguro, M. Fujita, M. Sano, *J. Mol. Liq.* **2009**, *148*, 99; b) B. Doherty, X. Zhong, S. Gathiaka, B. Li, O. Acevedo, *J. Chem. Theory Comput.* **2017**, *13*, 6131; c) Y.-L. Wang, F. U. Shah, S. Glavatskih, O. N. Antzutkin, A. Laaksonen, *J. Phys. Chem. B* **2014**, *118*, 8711.